Finger-like patterns in sedimenting water–sand suspensions

C. Völtz[a],*, M. Schröter[a], G. Iori[b], A. Betat[a], A. Lange[c], A. Engel[c], I. Rehberg[a,1]

[a]*Institut für Experimentelle Physik, Otto-von-Guericke-Universität, PF 4120, D-39016 Magdeburg, Germany*
[b]*Departament Estructura i Constituents de la Matèria, Universitat de Barcelona, Diagonal 647,
ES-08028 Barcelona, Spain*
[c]*Institut für Theoretische Physik, Otto-von-Guericke Universität, PF 4120, D-39016 Magdeburg, Germany*

Abstract

The temporal evolution of a water–sand interface driven by gravity is experimentally investigated. By means of a Fourier analysis of the evolving interface the growth rates are determined for the different modes appearing in the developing front. To model the observed behavior we apply the idea of the Rayleigh–Taylor instability for two stratified fluids. Carrying out a linear stability analysis we calculate the growth rates from the corresponding dispersion relations for finite and infinite cell sizes and compose those results with the experimental data. Alternatively, the situation of the sedimenting sand can be modeled by a two-dimensional cellular automaton. A qualitative similarity between that model and the experimental situation is obtained. © 2000 Elsevier Science B.V. All rights reserved.

PACS: 05.45. − a

1. Introduction

There has been great interest in the behavior of granular materials over the last years (for a review see [1] and references therein). Examples for the surprising behavior of granular matter are two-dimensional localized states, called oscillons [2], in vertically vibrated containers, stratification phenomena observed while pouring granular mixtures onto a pile [3] or singing sand audible in deserts [4].

In contrast to the amount of phenomena one lacks a sound theoretical explanation for the observations. Difficulties arise due to the highly complex, disordered structure formed by the grains

---

*Corresponding author. Universität Bayreuth, Physikalisches Institut, Experimentalphysik V, D-95440 Bayreuth, Germany.

[1] Present address: Universität Bayreuth, Physikalisches Institut, Experimentalphysik V, D-95440 Bayreuth, Germany.
E-mail address: camilla.voeltz@uni-bayreuth.de (C. Völtz).

and their nonlinear internal friction. Therefore, most theoretical approaches have been done by numerical methods. Molecular-dynamics simulations and cellular automata calculations are frequently applied, for recent reviews see [5]. These methods describe in some detail the interactions between the particular grains [6]. Conclusions on the macroscopic behavior of granular matter are then drawn from the simulations with a great number of particles. Despite the recent progress in computer performance the size of the systems is still too small for a quantitative comparison with real experiments [6,7].

Hydrodynamic approaches to granular material are few [8–11] and are associated with restrictions as no interparticle correlations [8], a Gaussian distribution in the velocity of the grains [9] or with smooth hard spheres at low density [11]. Nevertheless, there are striking phenomenological similarities in the observed patterns for pure granular materials and pure fluids. Experiments with an inclined chute [12,13] or a vertically vibrated container [14,15] show the most notable analogy. In the latter experiments one observes for not too large driving frequencies that a solid–fluid transition can be detected. The second transition to hydrodynamic surface waves is associated with this fluid-like behavior of the layer of pure granular material.

Pure granular assemblies are characterized by the existence of a network of particles *in contact*. At these contacts the forces are transmitted, resulting in a *nonuniform* force network across the granular assembly. This force network accounts for a behavior different from ordinary fluids. Among the unusual effects are the pressure drop in the center beneath a pile of pure granular material, the effect of arching in a filled vessel, or the occurrence of the fastest flow in thin layer near the wall during the unloading of a hopper. It is clear that granular media are different from pure fluids but under certain conditions these differences are *not prevailing*. For example, the addition of an interstitial fluid may change the behavior of the composed system with respect to pure, i.e. dry, granular materials.

The flow of grains embedded in an interstitial fluid is dominated either by the effects of grain inertia or by effects of fluid viscosity. The Bagnold number B [16] expresses the ratio of collision forces between the grains to viscous forces in the fluid–grain mixture.[2] A small Bagnold number, $B < 40$, characterizes the regime of the macro-viscous flow. In this regime the viscous interaction with the pure fluid is important. Examples for this type of flow are mud slides and the transport of water–sand mixtures in river beds. At large Bagnold numbers, $B > 450$, the flow is called grain-inertia regime where the grain–grain interactions dominate. All flows of grains with air as interstitial fluid fall into the grain–grain regime.

Here, experiments are performed with sand dispersed in water both filled in a cell. By rotating the cell the sand is layered above the water which leads to a gravitational instable situation. Therefore the sand starts to sediment. The occurring shear rates, the mean particle diameters, and the viscosity of water result in a Bagnold number of about 1 [17]. This motivates the idea to consider the water–sand mixture as fluid-like. In the experiments we observe that the initial flat water–sand interface evolves into a finger-like pattern. The measured velocity for the largest finger was typically three times the Stokes velocity of a settling hard sphere. Furthermore, the velocity was

---

[2] The Bagnold number is defined as $B = \sqrt{\lambda}\rho_{grain}d^2\dot{\gamma}/\eta_{fluid}$. Here d is the diameter and ρ_{grain} the density of the grains. The shear rate is denoted by $\dot{\gamma}$ and η_{fluid} is the interstitial kinematic fluid viscosity. The 'linear concentration' λ introduced by Bagnold [16] is related to the packing density.

nearly independent of the mass of the sand and the diameter of the particles [17]. This independence of particle properties encourages a fluid-like description of the water–sand mixture. To model this behavior we test a continuum approach which is based on a well-known hydrodynamic instability.

The aim is to determine the critical parameters for the stability of the pattern and the dispersion relation for the *whole* spectrum of wave numbers detectable in the experiment. Particularly, the latter extends significantly the objectives of earlier experiments with water and polystyrene spheres [18] and with water and glass beads [19].[3] The dependence of the initial wavelength of the developing pattern on the width of the cell was studied in [18]. In [19] the experiments were focused on the evolution of voidage shock fronts caused by a step increase or decrease in the fluidization velocity for a fluidized bed. We, however, turn our attention to the temporal evolution of *all* wave numbers.

To model the water–sand mixture as a Newtonian fluid with effective properties depending on the concentration of the particles is obviously a simplifying description. In such a model it is assumed that the particle concentration in the flowing mixture is almost constant. Furthermore, the particles have to be large enough to neglect their Brownian diffusion. In the clear knowledge of the limitations of a fluid model for the water–sand mixture we will examine whether such an approach can catch the essence of the experimental results.

Whereas the fluid approximation leads to a *quantitative* comparison for all wave numbers, simulations by means of a cellular automaton aim at a different aspect. The purpose is to generate patterns with the same *qualitative* features as those seen in the experiment. The used automaton is restricted to a two-dimensional lattice where reflecting walls and no slip boundary conditions are imposed.

In the following section, the experimental arrangement is described and the results for the growth rates of the wave numbers are presented. In Section 3 the model is explained and thereafter the cellular automaton (Section 4). The calculated growth rates are compared with those of the experiment in Section 5. Section 6 contains our conclusions and some remarks about further prospectives.

2. Experiment

2.1. Experimental setup

A closed Hele-Shaw-like cell is used to investigate the temporal evolution of a water–sand interface driven by gravity (see Fig. 1). Cells of different widths but constant length (99.2 mm) and height (50 mm) are used. The cell is filled with sand and distilled water. As sand we use spherical glass particles (Würth Ballotini MGL) with a material density of 2.45 g/cm^3 and a size distribution of 63–71 μm. The cell is revolved by a stepping motor. The motor rotates the cell in 233 ms. The rotation axis is in the plane of the interface. This minimizes the centrifugal forces on the sand layer

---

[3] We are referring especially to the experimental runs where an initially unsaturated bed of beads was suddenly exposed to a high velocity fluid.
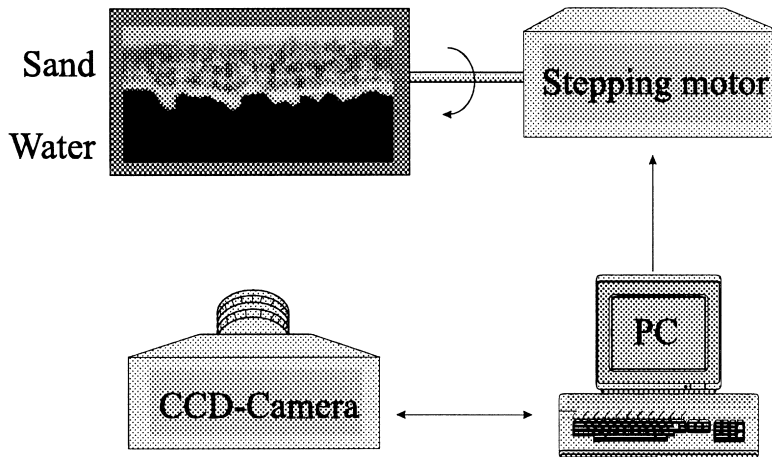
Fig. 1. Experimental setup.

while the cell is turned. The immovable camera which is fixed to the laboratory frame starts to take snapshots 545 μs after the cell is turned upside down. The time of the first snapshot defines the starting time $t = 0$. The images have a dimension of 256×364 pixel. To achieve a reasonable resolution we only focus on a horizontal length of 29.35 mm at the middle of the cell. The resolution in this setup is given by 12.4 pixel/mm.

After each rotation the suspension sediments until all particles are settled. This process takes typically less than 1 min. Therefore, a waiting time of about 1 min between consecutive runs is sufficient for the flow in the cell to come to rest.

2.2. Determination of the experimental parameters

Fig. 2 shows typical images of the sand–water cell at certain stages. Eighty milliseconds after the series of snapshots is started, the initial flat sand layer (Fig. 2a) is modulated at small scales (Fig. 2b and c). These disturbances are enhanced and give rise to sand fingers as seen in Fig. 2d and e. At later stages the fingers evolve to a mushroom-like pattern (Fig. 2f). This type of pattern was also found by numerical simulations for two stratified suspensions of different concentration [20] as well as for two fluids of different density [21].

The rotation of the apparatus leads to an interface which is not perfectly flat even in the beginning of the flow process. This results in three-dimensional flow effects which are studied in detail. The setup was modified in such a way that pictures of the side view into the cell could be taken. The pictures manifest that during the rotation the heavier fluid starts to slide. This effect is increased during the time interval of slowing down due to the inertia of the heavier fluid. When the rotation is finished the sliding has moved parts of the heavier fluid to the back wall of the cell (with respect to the camera) resulting in an inclined interface (see Fig. 3a). Now, the heavier fluid slides along the back wall and from there it flows towards the front wall (see Fig. 3b). Obviously, the flow in thick cells cannot be described as a pure vertical sedimentation and convection across the cell width is likely. These effects die out in thin cells which can be seen in Fig. 3c.
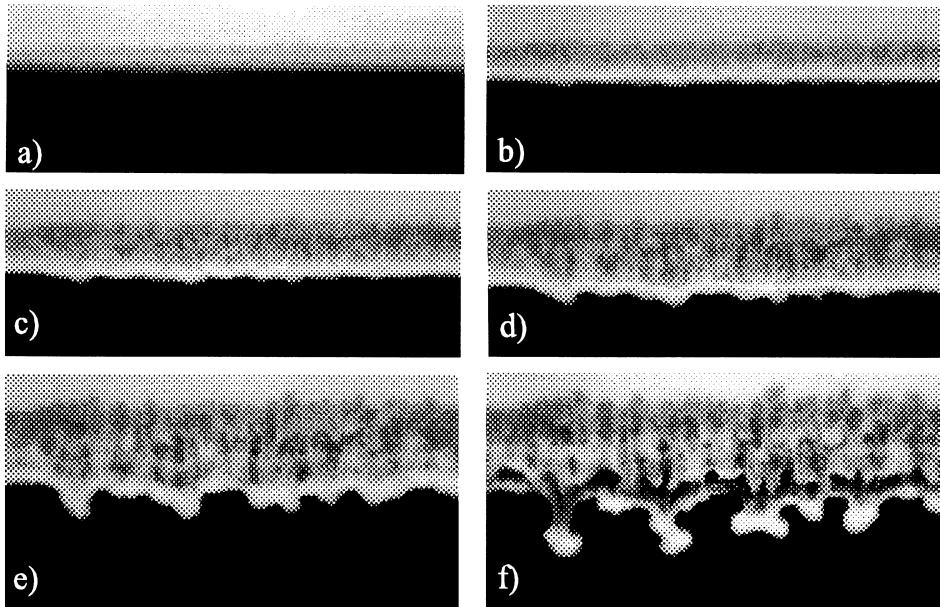
Fig. 2. Sand–water interfaces at certain time steps: (a) 0 ms, (b) 80 ms, (c) 120 ms, (d) 160 ms, (e) 200 ms and (f) 240 ms. The size distribution of the sand particles is given by 63–71 μm and the sand mass in the cell by 2.02 g, respectively. The presented frames show the middle part of the cell and have a horizontal length of 29.35 mm (cell width 2 mm).
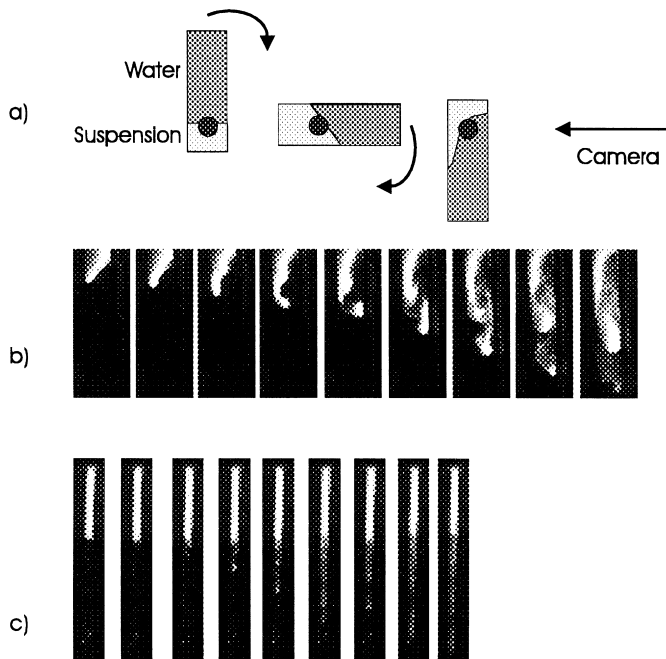

Fig. 3. (a) Sketch of the sliding process during the rotation of the cell. The axis of rotation is indicated by a filled black circle. (b,c) Side view of the cell at different times and for cell widths of 4.3 mm (b) and 1.0 mm (c). Three-dimensional flow phenomena appear in thick cells (b) and can be suppressed in thin cells (c). The time interval between consecutive images is 80 ms where the first picture is taken at 40 ms.
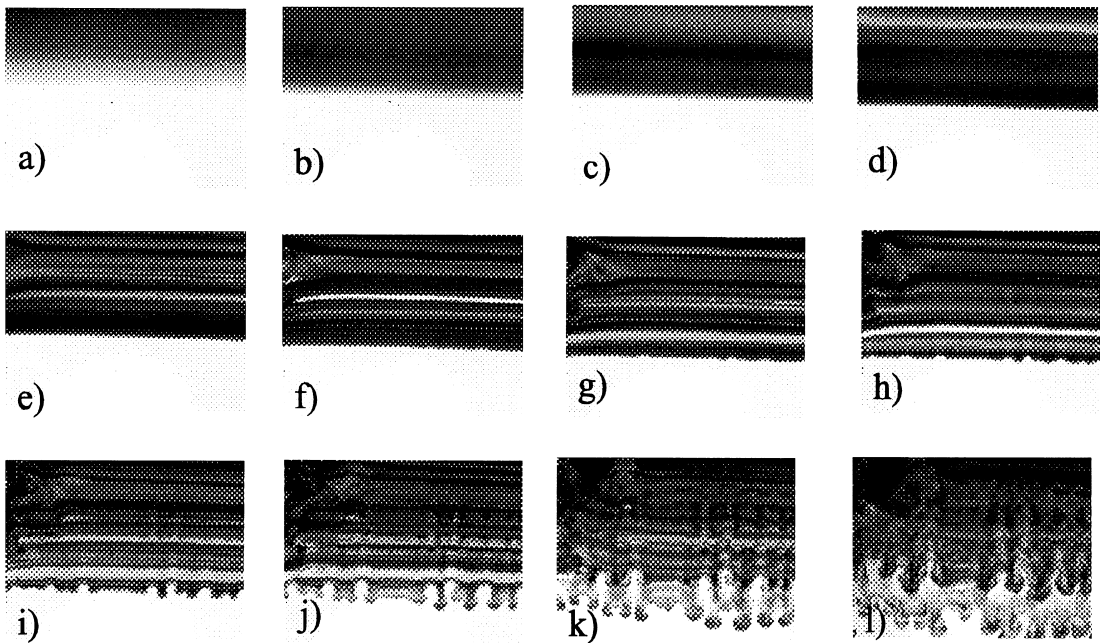
Fig. 4. Salt–fresh water interfaces at time $t = 0, 80, 120, 160, 200, 240, 280, 320, 360, 400, 480$ and 560 ms (a–l). About 120 ms after the sedimentation started, light horizontal stripes appear (d). At later stages (h–k) a typical finger pattern evolves. The cell width is 3.5 mm and the density of the dyed saturated salt water ~ 1.19 g/cm^3, respectively. The presented frames show the middle part of cell and have a horizontal length of 32.6 mm.

Several tests are performed in which the cell width and the density difference between the two media are varied in order to study their influence on the three-dimensional flow effects. Since a continuous variation of the density of the sand is hard to realize, dyed NaCl solutions of different densities are used as the heavier fluid. In one set of experiments (cell width 3.5 mm) a saturated NaCl solutions ($\rho \sim 1.19$ g/cm^3) is layered above fresh water. The evolving interface shows the surprising phenomenon of light horizontal stripes whose number increases with increasing time (see Fig. 4). The appearance of these stripes can be explained with the assumption of a three-dimensional flow. The stripes are caused by flow components across the cell width. These components transport fresh water to the back wall of the cell leading to layers across the cell completely filled with fresh water. These layers can be seen as light horizontal stripes. Similar patterns were observed in [22].

By reducing the cell width to 0.5 mm and the density difference to $\Delta\rho \sim 0.028$ g/cm^3 no three-dimensional effects could be observed (see Fig. 5). Obviously, smaller widths approximate better a two-dimensional system. Due to the role of inertia of the heavier fluid sliding effects are less pronounced for fluids with smaller density differences.

In order to prove that the convection is purely driven by three-dimensional flow effects, the thermal influences on the convection was also tested. Therefore, in a control experiment the cell was heated from the front side. The resulting convection rolls appear on a very large time scale compared to the rotational triggered ones. Therefore, a thermal triggered convection, as suggested in [23], can here be excluded.
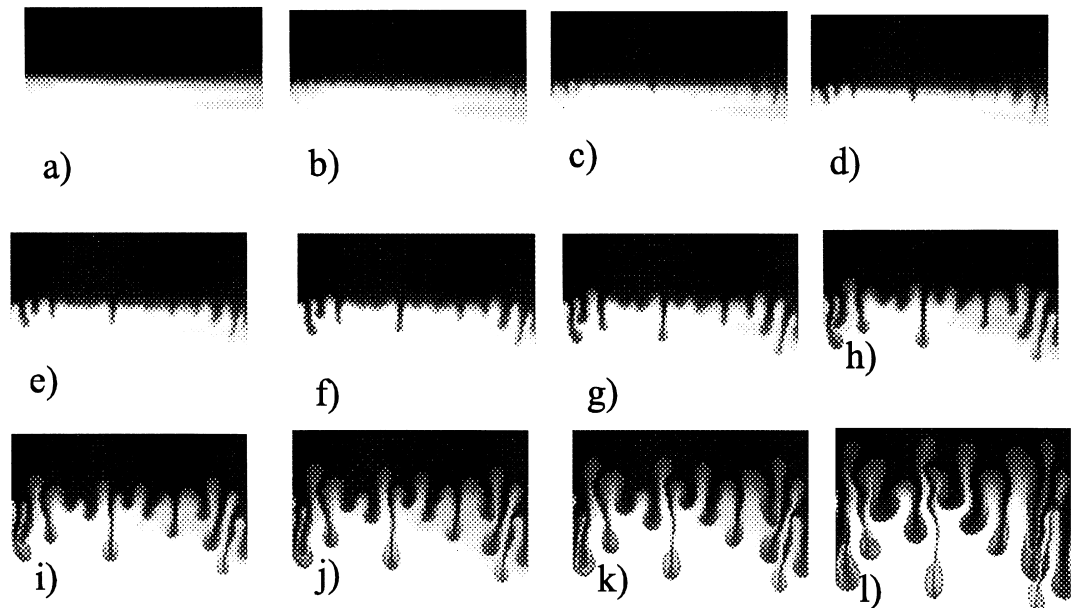
Fig. 5. Salt–fresh water interfaces at time $t = 0, 4.8, 5.4, 6.0, 6.6, 7.2, 7.8, 8.4, 9.0, 9.6, 10.2,$ and $11.4\,s$ (a–l). No light horizontal stripes appear, e.g. no three-dimensional flow effects. Beginning with small undulations (b), a finger-like pattern develops (c–f) followed by plume-like structures (g–l). The cell width is 0.5 mm and the density of the dyed salt water ~ 1.028 g/cm^3, respectively. The presented frames show the middle part of the cell and have a horizontal length of 32.9 mm.

For experiments with water and granular material the first condition for a two-dimensional flow can be easily realized. The second condition is difficult to accomplish because granular material with a density close to water, e.g. polystyrene beads ('Vernetztes Styrol-Perlpolymerisat', BAYER, size distribution 200–250 μm) with $1.0 < \rho < 1.1$ g/cm^3, shows strong electrostatic charge effects. Even by adding of surfactants the charge effects could not be completely avoided. Therefore, a cell of 2 mm width and spherical glass particles (Würth Ballotini MGL) present the best choice with respect to a two-dimensional fluid-like flow and visibility.

For cells thinner than 2 mm several problems occur and were studied. The images in Fig. 6 show that initial disturbances develop into sand fingers of notable smaller size and less pronounced mushroom-like pattern compared with the patterns obtained in wider cells (see Fig. 2). We even observe pinchoff effects at the fingers tips (see image at $t = 240$ ms in Fig. 6). More experiments with thin cells were performed to investigate how the sedimentation process depends on the initial packing density. Preparing the system with a high initial packing density leads to a compacted, more solid-state-like sediment rather than a fluid-like mixture. The observed type of sedimentation process is characterized by the sinking of individual particles out of the compacted sediment (see Fig. 7). Therefore, a continuous fluid-like downflow cannot be observed for higher initial packing densities. A reason for the observed discontinuous sedimentation could be arching effects which become relevant at high packing densities in thin cells. It is assumed that there is a critical initial packing density which separates a fluid-like downflow from a particle-like downflow (cf. Fig. 7 and the fifth frame in Fig. 6).
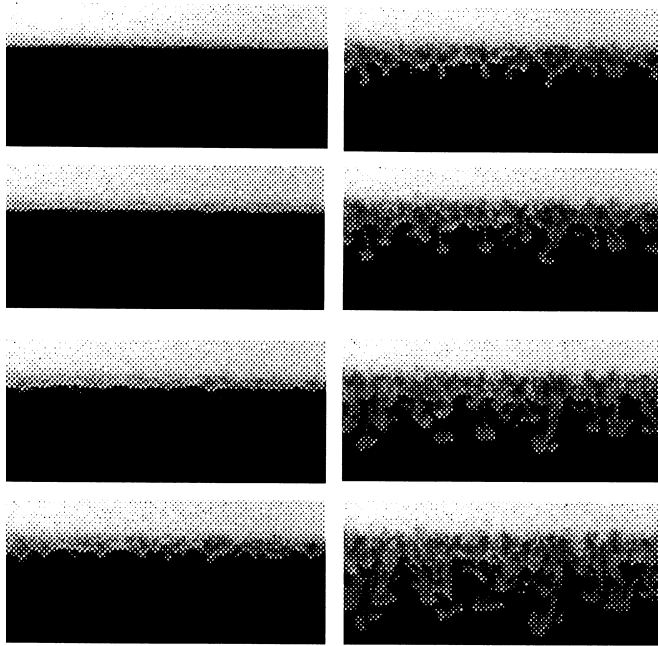
Fig. 6. Sand–water interfaces at time steps of 40 ms commencing with $t = 0$. The sand fingers are of notable smaller size and the mushroom-like pattern is less pronounced compared with the patterns obtained in a wider cell (see Fig. 2). The size distribution of the sand particles is given by 80–90 μm and the sand mass in the cell by 2 g, respectively. The presented frames show the middle part of the cell (width = 1 mm) and have a horizontal length of 26.7 mm.

Fig. 7. Snapshot of the sedimentation with a *high* initial packing density at $t = 160$ ms. Because only individual particles come out of the sediment the pattern appears dim. The cell parameters are as in Fig. 6 with the exception of the horizontal length, which is now 29.6 mm.

2.3. Experimental results

The system for the determination of the growth rates was prepared in the following way: a cell of 2 mm width (height 50 mm, length 99.2 mm) is filled with 2.02 g of spherical glass particles with a size distribution 63–71 μm. The used resolution is 12.4 pixel/mm. The total number of evaluated runs is 52. Fig. 2 shows a typical sequence of images during the sedimentation.

To analyze this sequence we apply a threshold algorithm to obtain the water–sand interface. We look at every column of our digitized image to determine the point where the gray scale exceeds a certain value. We start at the bottom (water) and continue to the top (sand). In this way, we track down the interface of the pattern. Fig. 8 shows the temporal evolution of the images presented in Fig. 2. Here the interfaces of all patterns are shown. While our detecting method works for the patterns during the first stages, namely small-scale modulations and sand fingers, it breaks down
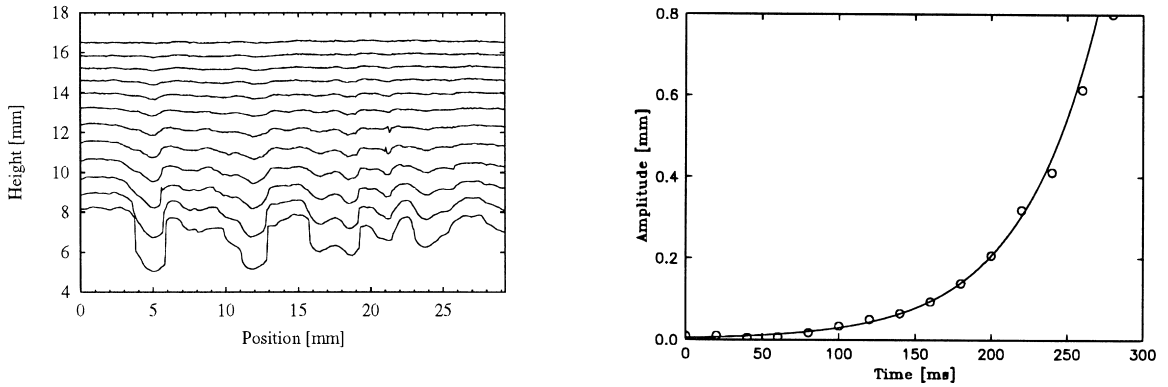
Fig. 8. Temporal evolution of the water–sand interfaces. The patterns are detected every 20 ms and shown with a constant vertical offset of 0.5 mm. The experimental conditions are the same as in Fig. 2.

Fig. 9. Amplitude A of a DFT-analysis for a typical wave number (here $k \simeq 4.3 \, \mathrm{cm}^{-1}$) in dependence on time t. An exponential fit is obtained by Eq. (1). The values belong to the interfaces presented in Fig. 8.

for mushroom-like patterns. However, this is not crucial because those patterns are beyond the scope of the linear analysis presented here. Discrete Fourier transformation (DFT) gives the Fourier spectrum of each interface. Fig. 9 shows the temporal evolution of the amplitude A of a typical Fourier mode. It is seen that A grows exponentially from the first image to $t \sim 270$ ms. By an exponential fit

$$A(k) = A_i(k) \exp(n(k)t) , \tag{1}$$

we obtain the growth rate n for every wave number k in our spectra, where A_i is the initial amplitude. For each fit it was monitored that $A(k)$ was smaller than 40% of its wavelength, the criterion for the linear regime [24].

In order to test the reliability of our experimental setup we perform 52 independent runs with one set of material parameters. These 52 measurements are analyzed to obtain a mean initial amplitude for each wave number. It is seen that the initial amplitude decreases for increasing wave numbers (see Fig. 10). In the case of large wave numbers we do not obtain *exponential* fits for every experimental run. This is due to the fact that the amplitude is very small and that we approach the limit of the resolution of our image processing. The error bars in Fig. 10 indicate that the number of runs which can be analyzed decreases for larger wave numbers.

An obvious question concerning the underlying mechanism of the pattern formation in our system is: How do different material parameters effect the dispersion relation? Therefore, we carry out experiments with different material configurations which are characterized in Table 1. The used setup is different where the cell and the CCD-camera are fixed to a frame which is resolved by hand (for details see [25]). Using 2, 4 and 8 g of sand (Experiments I–III) we observe a shift of all growth rates towards larger values with increasing mass of sand. This effect is independent of the wave number (Fig. 11a). Using three different size distributions (Experiments I, IV, V) the ratio of the cell thickness of 4 mm to the mean particle diameter varies between ~ 70 and ~ 40. As Fig. 11b shows this variation of the mean particle diameter does not have a significant influence on the dispersion
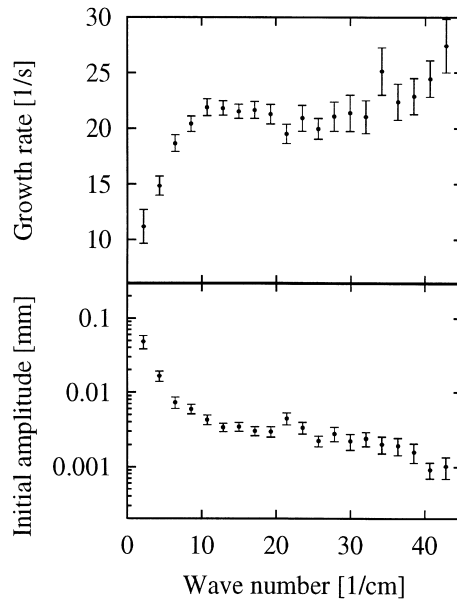
Fig. 10. Growth rate (top) and initial amplitude (bottom) versus the wave number k. A cell of 2 mm width (height 50 mm, length 99.2 mm) is used with 2.02 g of spherical glass particles with a size distribution 63–71 μm. The error bars are given by the standard deviation of the mean value.

Table 1
Details of sand used in certain experimental configurations

Experiment	Size distribution (μm)	Mass (g)	Runs
I	71–80	2	100
II	71–80	4	12
III	71–80	8	12
IV	56–63	2	12
V	90–100	2	12

relation $n(k)$. As a common feature we find the same overall behavior for all material sets: The growth rates increase for small k and reach a plateau for larger values of k.

3. Theory

We choose a two fluid system as a model to describe the experimental results. In the initial state two incompressible fluids of constant densities ρ_1 and ρ_2 and constant dynamical viscosities μ_1 and μ_2 are arranged in two horizontal strata. Index 1 (2) refers to the fluid at the bottom (top) of
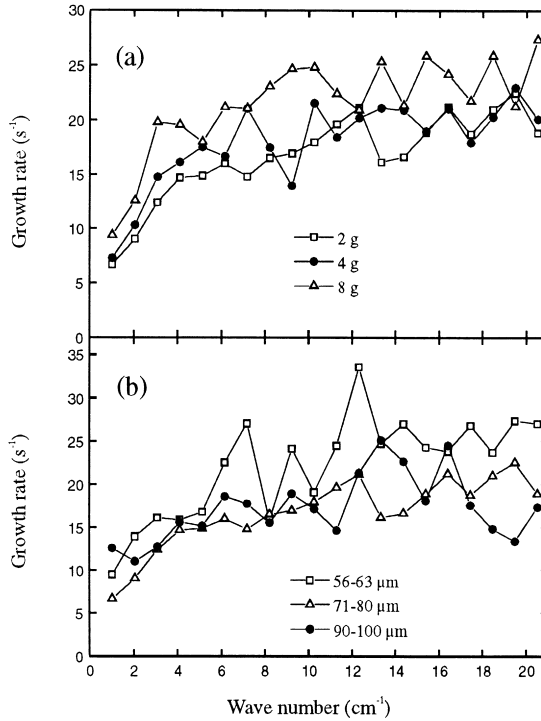
Fig. 11. Growth rate versus the wave number for different material parameters. In (a) 2 g ($\square$), 4 g ($\bullet$), and 8 g ($\triangle$) of sand with the same size distribution were used (Experiments I–III). In (b) 2 g of sand with size distributions of 56–63 μm ($\square$), 71–80 μm ($\triangle$), and 90–100 μm ($\bullet$) were used (Experiments IV, I, V).

the system. The pressure is a function of the vertical coordinate z only; x and y are the coordinates in the plane perpendicular to z. The acceleration due to gravity acts in negative z direction. A *linear* stability analysis is carried out for small disturbances of this initial state. The instability of a planar interface $z = z_s(x, y) \equiv 0$ between the two fluids is known as the Rayleigh–Taylor instability [24,26,27].

We assume that the boundaries in the z direction are far from the interface. Small changes δz_s in the form of the interface cause a pressure difference which is balanced by the product of the surface tension T_s and the curvature of the interface. Considering small disturbances $\delta\rho$ in the density and δp in the pressure the Navier–Stokes equations read [27]

$$\rho\partial_t u = -\partial_x \delta p + \mu\Delta u + (\partial_x w + \partial_z u)\partial_z\mu , \tag{2}$$

$$\rho\partial_t v = -\partial_y \delta p + \mu\Delta v + (\partial_y w + \partial_z v)\partial_z\mu , \tag{3}$$

$$\rho\partial_t w = -\partial_z \delta p + \mu\Delta w + 2\partial_z w\partial_z\mu - g\delta\rho + T_s(\partial_x^2 + \partial_y^2)\delta z_s\delta(z - z_s) , \tag{4}$$

where $\partial_i = \partial/\partial_i$, $i = x, y, z, t$. The z dependence of μ gives rise to the third term on the right-hand side of (2)–(4) since the viscous part in the Navier–Stokes equations is $\partial_j[\mu(\partial_j v_i + \partial_i v_j)]$ for an incompressible fluid. For convenience, we adhere to $\partial_z\mu$ though $\partial_z\mu$ is different from zero only at

the interface. The components of the velocity field $\boldsymbol{v}$ are $v_x = u$, $v_y = v$, and $v_z = w$ and are considered small, so that Eqs. (2)–(4) contain only terms which are linear in the disturbances. The delta function $\delta(z - z_s)$ ensures that the surface tension appears at the interface z_s between the two fluids. The equation of continuity (mass conservation) for an incompressible fluid is

$$\text{div}\, \boldsymbol{v} = \partial_x u + \partial_y v + \partial_z w = 0 \,. \tag{5}$$

Additionally, the equation

$$\partial_t \delta\rho = -(\boldsymbol{v}\,\text{grad})\rho = -w\partial_z \rho \tag{6}$$

relates the temporal variations in the density fluctuations to the density jump at the interface which moves with w in the z direction. Eqs. (2)–(6) govern the linearized system. The disturbances are analyzed to as *normal modes* thus seeking solutions which x and t dependence is proportional to $\exp(ikx + nt)$. The wave number is denoted by k and $n(k)$ is the growth rate of the corresponding mode k. If the fluid is confined between two rigid planes the boundary conditions are

$$w = \partial_z w = 0 \quad \text{at}\ z = \pm\infty \,, \tag{7}$$

where we shift the planes to infinity for the sake of simplicity. The other boundary conditions are related to the interface. All three components of the velocity and the tangential viscous stresses must be continuous. Using the exponential ansatz for the continuous velocity components, Eq. (5) gives the continuity of $\partial_z w$, too. The continuity of $\mu(\partial_z^2 + k^2)w$ is the condition which ensures that the two tangential stress components are continuous across the interface. Inserting the exponential ansatz into (2)–(6) and determining the solution of w in each region in such a way that the boundary condition (7) as well as the interfacial conditions are satisfied leads to the dispersion relation [27]

$$-\left\{\frac{gk}{n^2}\left[(\alpha_1 - \alpha_2) + \frac{k^2 T}{g(\rho_1 + \rho_2)}\right] + 1\right\}(\alpha_2 q_1 + \alpha_1 q_2 - k) - 4k\alpha_1\alpha_2$$

$$+ \frac{4k^2}{n}(\alpha_1 v_1 - \alpha_2 v_2)[\alpha_2 q_1 - \alpha_1 q_2 + k(\alpha_1 - \alpha_2)]$$

$$+ \frac{4k^3}{n^2}(\alpha_1 v_1 - \alpha_2 v_2)^2 (q_1 - k)(q_2 - k) = 0 \,. \tag{8}$$

The abbreviations $\alpha_{1,2} = \rho_{1,2}/(\rho_1 + \rho_2)$ and $q_{1,2}^2 = k^2 + n/v_{1,2}$ were introduced where $v_{1,2} = \mu_{1,2}/\rho_{1,2}$ is the kinematic viscosity for each region. For the rest of the paper we will use a dimensionless surface tension $S = T/[(\rho_1 + \rho_2)(gv_1^4)^{1/3}]$ if not stated otherwise.

We now briefly discuss the general results of the dispersion relation (8). The configuration where the lighter fluid is on top of the heavier one, $\rho_2 < \rho_1$, is always stable, i.e., $\text{Re}\{n(k)\} \leq 0$ for all k. This is independent of whether there is any surface tension (Fig. 12b) or not (Fig. 12a). If the strata are in the opposite order, $\rho_2 > \rho_1$, then the surface tension plays a crucial role. In the case of no surface tension (Fig. 13a) the system is unstable against disturbances of any wave number, i.e., $\text{Re}\{n(k)\} \geq 0$ for all k. If there is a surface tension a critical wave number exists

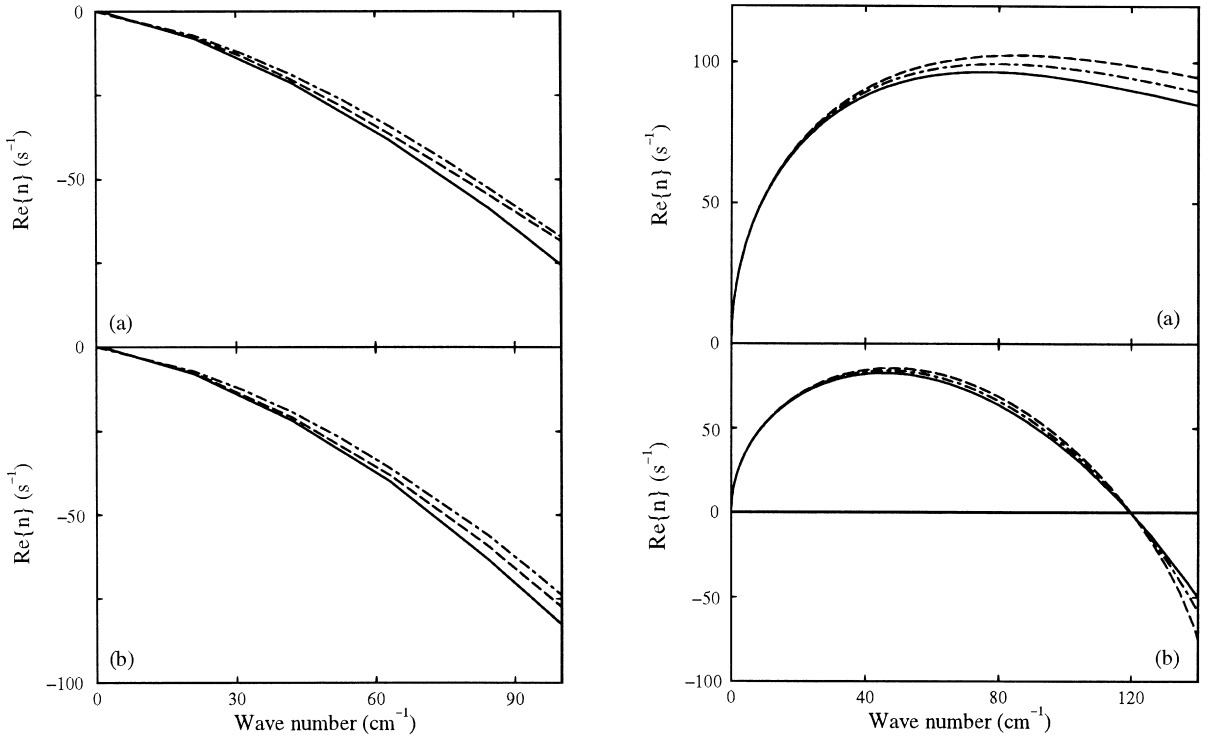$$k_c = \sqrt{\frac{g}{T}(\rho_2 - \rho_1)} \tag{9}$$

Fig. 12. For zero surface tension (a) and surface tension $S = 1$ (b) the growth rate $\text{Re}\{n\}$ of the modes is plotted versus their wave number k for the case that the top fluid is lighter than the bottom one, $\rho_2 = 0.5\rho_1$. The surface tension as well as the relation of the viscosities does not change the *overall* behavior too much as the three examples show: $v_1 = v_2 = 10^{-6}$ m²/s (solid line), $v_1 = 10^{-6}$ m²/s and $v_2 = 0.75v_1$ (long-dashed line), and $v_2 = 10^{-6}$ m²/s and $v_1 = 0.75v_2$ (dot–dashed line).

Fig. 13. The growth rate $\text{Re}\{n\}$ of the modes is plotted versus their wave number k for the case that the top fluid is heavier than the bottom one, $\rho_2 = 2\rho_1$. The surface tension S is zero in (a) and 1 in (b). The surface tension causes a drastic change in the behavior whereas the ratio of the viscosities does not change the *overall* behavior too much as the three examples show: $v_1 = v_2 = 10^{-6}$ m²/s (solid line), $v_1 = 10^{-6}$ m²/s and $v_2 = 0.75v_1$ (long-dashed line), and $v_2 = 10^{-6}$ m²/s and $v_1 = 0.75v_2$ (dot–dashed line).

and the system is stable (unstable) against modes with wave numbers which are larger (smaller) than k_c (Fig. 13b). A moderate variation in the relation between the two viscosities v_1 and v_2 has no strong influence on the general behavior of the growth rates (see Figs. 12 and 13).

The experiments are carried out in a finite-size cell in contrast to our simplification of infinite length in the z direction. We determine now the limits to which this simplification is justified (see also [28]). If the walls of the cell are at $z = \pm L_z$ the appropriate ansatz for w is

$$w_1 = a_1 e^{+kz} + a_2 e^{-kz} + b_1 e^{+q_1 z} + b_2 e^{-q_1 z} \quad \text{for } z \leq 0 , \tag{10}$$

$$w_2 = c_1 e^{+kz} + c_2 e^{-kz} + d_1 e^{+q_1 z} + d_2 e^{-q_1 z} \quad \text{for } z \geq 0 . \tag{11}$$
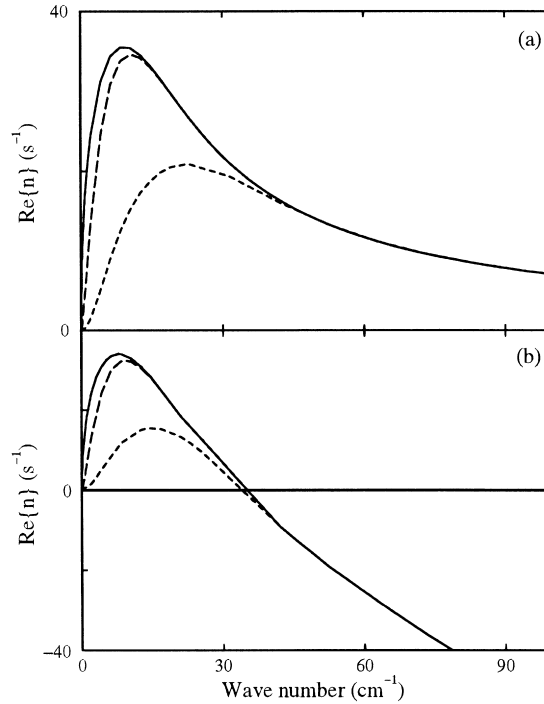
Fig. 14. For zero surface tension (a) and surface tension $S = 12.8$ (b) the growth rate $\mathrm{Re}\{n\}$ is plotted versus the wave number k for $L_z = \pm 3\,\mathrm{mm}$ (long-dashed line) and $L_z = \pm 1\,\mathrm{mm}$ (dashed line). For comparison the solid line shows the graph for infinite L_z. It reveals that finite-size effects play a significant role if $k < 2\pi/|L_z|$. The material parameters are $\rho_2 = 2\rho_1$ and $\nu_2 = 33\nu_1$ with $\rho_1 = 1\,\mathrm{g/cm^3}$ and $\nu_1 = 10^{-6}\,\mathrm{m^2/s}$.

With the boundary condition $w = \partial_z w = 0$ at $z = \pm L_z$ and the analysis at the interface as above one ends up with a system of eight equations for the constants in (10) and (11). The coefficients of the corresponding matrix are given in the appendix. The vanishing determinant leads to the dispersion relation $n(k)$, its numerical solution is shown in Fig. 14 for different lengths L_z. The comparison with the data for infinite L_z shows that there is no real difference as long as $|L_z| > 3\,\mathrm{mm}$ for the used material parameters. Since the thickness of the sand layer is below this margin we expect finite-size effects. In the case of asymmetrically arranged walls at $z = -L_1$ and $+L_2$ the dispersion relation shows up to a ratio of $|L_1|/L_2 \simeq 17$ only a very weak deviation from the results for symmetrical walls.

In the frame of our continuum approach we consider the water–sand mixture as a suspension in accordance with the classification in [29]. The dispersion medium is water and the dispersed material consists of sand particles with a mean diameter and a density as stated in Section 2. The material density as well as the dynamical viscosity of the mixture depend on the packing density ϕ of the granular material. The packing density ϕ measures the volumetric concentration of the particles in the mixture. The material density of the mixture is given by

$$\rho_{\mathrm{mixture}} = \phi\rho_{\mathrm{sand}} + (1 - \phi)\rho_{\mathrm{water}} \ . \tag{12}$$
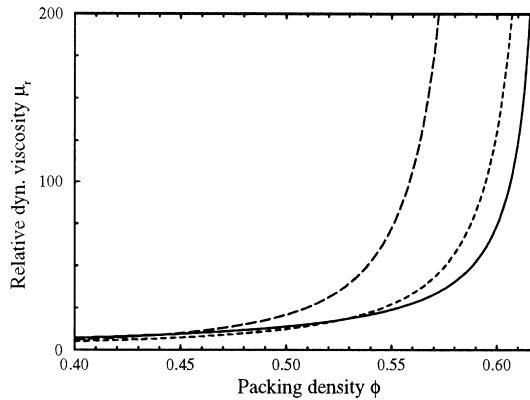
Fig. 15. Relative dynamical viscosity μ_r versus the packing density ϕ. The results of the three empirical formula (13)–(15) are plotted as dashed, long-dashed, and solid lines. μ_r is nearly the same for all three approaches provided the packing is not too dense, $\phi \leq 0.48$. Above this range μ_r starts to diverge as ϕ reaches ϕ_{max} where the divergent behavior differs significantly between the various approximations.

Since ρ_{water} and ρ_{sand} are constant, the considered small disturbances in the mixture density $\delta\rho_{mixture}$ imply that ϕ varies according to Eq. (12). In the following, index 1 refers to water and 2 to the mixture, respectively. Three empirical formulae [30–32]

$$\frac{\mu_2}{\mu_1} = \mu_r = \left(1 - \frac{\phi}{\phi_{max}}\right)^{-2.5\phi_{max}} \qquad \text{with } \phi_{max} = 0.63 , \tag{13}$$

$$\frac{\mu_2}{\mu_1} = \mu_r = \left(1 + \frac{0.75}{(\phi_{max}/\phi) - 1}\right)^2 \qquad \text{with } \phi_{max} = 0.605 , \tag{14}$$

$$\frac{\mu_2}{\mu_1} = \mu_r = \frac{1}{[1 - (\phi/\phi_{max})^{1/3}]} \qquad \text{with } \phi_{max} = 0.625 \tag{15}$$

were widely used for the dynamical viscosity of a hard sphere suspension. The maximal packing densities in (13), (14) result from the fit of the proposed formulae to the experimental results.

Fig. 15 shows the behavior of the relative dynamical viscosity μ_r for different packing densities ϕ according to Eqs. (13)–(15). All three of them give nearly the same value for $\mu_r(\phi)$ at moderately dense packings, $0.4 \leq \phi \leq 0.48$. Above this region the relative viscosity diverges as ϕ approaches its maximal value. But the strength of the divergent behavior is remarkably different so that μ_r already varies about a factor of 5 for $\phi = 0.57$. The fact of wide spread measured values for the relative viscosity of the same system is exemplary shown in [33]. The measured values of μ_r vary between 21 and 400 for a rather colloid system at $\phi \approx 0.5$. A similar situation is present for suspensions [34] which is why we cannot rely on a fixed value of μ_r within small error bars. Therefore, we consider μ_r a variable parameter within reasonable limits rather than a fixed material parameter.

4. Cellular automaton

The evolution of the sedimentation process is investigated numerically by a two-dimensional computer model, which combines elements of a cellular automaton and a lattice-gas approach. It keeps track of both the location of individual sand grains and of the fluid flow in a simplified way: the interaction between the sand and water is described by Stokes law, and the velocity of the water flow is determined by Darcy's law, thus taking into account the Hele-Shaw geometry used in the experiment.

A layer of sand particles is initially placed at the top of a rectangular lattice of size $L1 \times L2$. The particles move under the influence of the gravitational force and the water flow. The velocity of sand is evaluated in parallel and the position of all particles is updated at any time step. If a sand particle reaches a position which is already occupied by another grain it is not allowed to stop there – instead it diffuses around that point until it finds an empty space. Reflecting walls for the particles are chosen as simplified boundary conditions.

The fluid velocity is evaluated imposing Darcy's law and the equation of continuity. The vertical component of the water velocity is proportional to the local density of particles $\rho(x, z)$. According to the equation of continuity in two dimensions, the integral $\int w \, dx$ must be zero. Therefore, if the local density at a specific point is higher (lower) than the average density along that horizontal coordinate, $\bar{\rho}(z)$, the water velocity is directed downward (upward) and its magnitude is

$$w_{\text{water}}(x, z) = \alpha[\rho(x, z) - \bar{\rho}(z)]$$

with a free parameter α, which represents the permeability of the Hele-Shaw cell. The local density at a given point is given by the number of sand particles inside a square box of side l around that point. The horizontal component of the water velocity is then calculated by imposing

$$\partial_x u_{\text{water}} + \partial_z w_{\text{water}} = 0 \, , \tag{16}$$

the equation of continuity in the two-dimensional cell.

Once the fluid velocities are known at any point of the lattice the displacement of the sand particles are determined applying the rules

$$d_t x_{\text{p}} = u_{\text{water}} \, ,$$

$$d_t z_{\text{s}} = w_{\text{water}} + v_{\text{g}} \, , \tag{17}$$

where v_{g} is the Stokes velocity of the particles determined by the gravitational field.

In Fig. 16 the results of a simulation with 22 800 sand particles on a horizontal lattice of size $L1 = 400$ are shown with the following parameters: $l = 6$, $v_{\text{g}} = 4$, $\alpha = 0.1$, and an initial density of 0.95 for the sand. The snap-shots from top to bottom refer to later stages of the dynamics. Finger-like structures with higher density at the tips develop at the beginning of the sedimentation process. Considering the simplicity of the model, the qualitative similarity with Fig. 2 can be considered as striking. We thus believe that the model catches the essence of the physical mechanisms involved in this pattern forming process.
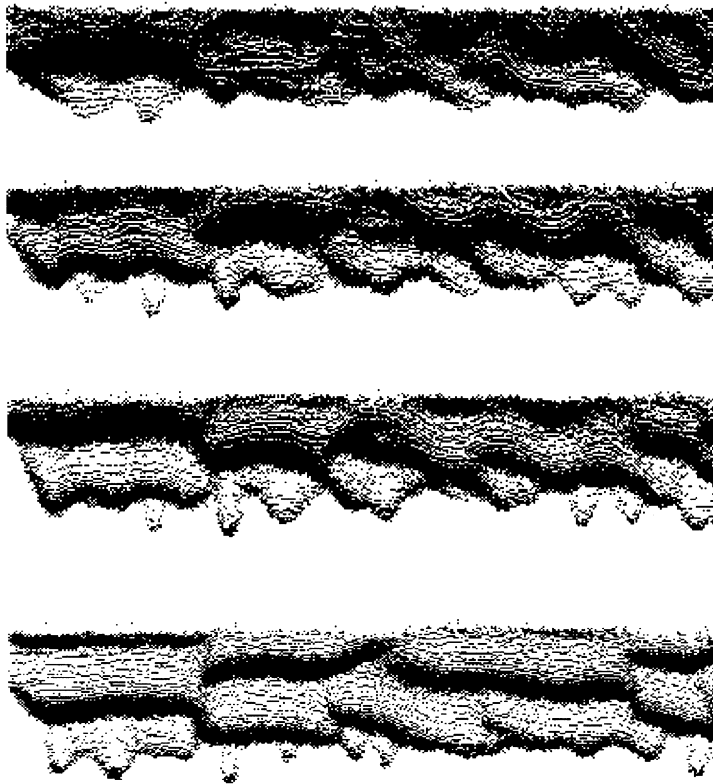
Fig. 16. Sedimenting fingers simulated by means of a cellular automaton. Finger-like structures with higher density at the tips evolve at the beginning of the sedimentation. Each snapshot shows the whole horizontal lattice size of $L1 = 400$. The other parameters are: $l = 6$, $v_g = 4$, $\alpha = 0.1$, and 0.95 for the initial density of the sand.

5. Results and discussion

The experiments are carried out in a system as described in the first paragraph of Section 2.3. The height of the sedimented sand layer was measured to 6.8 ± 0.1 mm where the error corresponds to a confidence interval of 95%. This results in a packing density of $\phi = 0.61 \pm 0.04$ where the error is given by the standard deviation of the mean value. Thus, the mixture is sufficiently characterized by Eqs. (12)–(15) where $\rho_{\text{water}} = 0.988$ g/cm^3. By means of (15) the viscosity of the mixture is $\mu_2 \simeq 104\mu_1$ for $\phi \simeq 0.607$ which gives together with an effective height of the fluidized layer of $L_z = 2.1$ mm the best fit with the experimental data. The height of the fluidized sand layer was determined by analyzing the snapshot at $t = 0$. There is a clear first drop in the mean gray value at a height of $\simeq 18.3$ mm (see Fig. 17). The drastic decrease in the mean gray value finishes at a height of $\simeq 16.2$ mm. We interpret the layer between both heights as the fluidized sand layer at $t = 0$ which enters into the calculations.

The resulting growth rates show a good agreement with the experimental data up to $k \sim 15$ cm^{-1} (Fig. 18). For larger wave numbers, the theory predicts a monotonous decrease of the
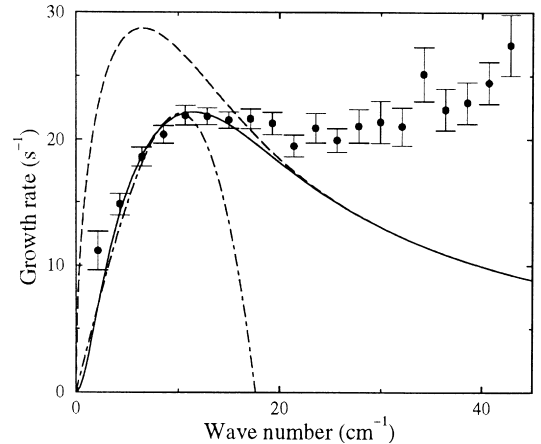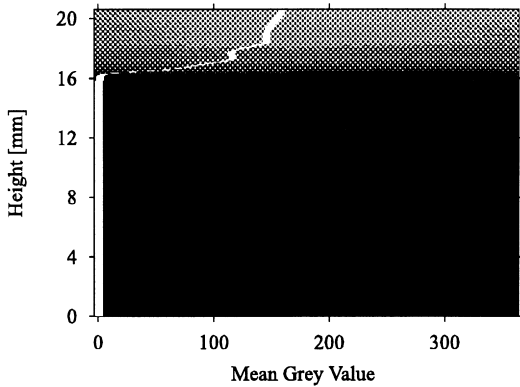
Fig. 17. Mean grey value (solid white line) from the top to the bottom across the cell at $t = 0$. The graph is calculated for the snapshot in the background of the figure.

Fig. 18. Growth rates n of the disturbances against their wave numbers k for a measured packing density of $\phi = 0.61$ (●). The theoretical results $n(k)$ are shown for $\mu_2 \simeq 104\mu_1$ at $\phi \simeq 0.607$ and different boundaries: $L_z = \pm \infty$ (long-dashed line) and $L_2 = 2.1$ mm, $L_1 = -43.2$ mm (solid line). The finite-size effects appear for small wave numbers and decrease with increasing wave numbers. The dot–dashed line presents the results of a Hele-Shaw cell of 2 mm width with $\mu_r \simeq 85$ at $\phi \simeq 0.603$ and $T \simeq 2.77 \times 10^{-3}$ N/m.

growth rate whereas the experimental growth rates display a weak increasing behavior. This means that the fluid-like model for a water–sand mixture works well at small wave numbers. We interpret the divergence at larger wave numbers as an indication that the model of a Newtonian fluid might not be appropriate for a suspension at large wave numbers.

Concerning the values of the packing density, we note that at a packing density of about $\phi = 0.61$ the effect of dilatancy occurs in order to allow the mixture to flow [35]. Therefore, we expect that more accurate measurements of the packing density during the sedimentation will lead to smaller packing densities. In Fig. 18 we calculate the dispersion relation for infinite as well as for finite boundaries, $L_2 = 2.1$ mm and $L_1 = -43.2$ mm. The finite-size effects appear for small wave numbers and decrease with increasing wave numbers. The dispersion relations for infinite and finite boundaries approach each other at wave numbers where the initial amplitudes of the disturbances are in the order of 7×10^{-3} mm. For these disturbances a boundary at 2.1 mm distance appears to be at infinity. Therefore for wave numbers beyond $k \sim 20$ cm^{-1} it does not matter whether we choose $L_z = \pm \infty$ or 2.1 mm. This is not the case for small wave numbers where the initial amplitudes reach an order of 10^{-1} mm (Fig. 10b).

The values for the viscosity of a water-sand mixture estimated in [19], $\mu_2 \sim (130–190)\mu_1$, are in a similar range as ours. These values are determined with the help of the *singular* wave number with the largest growth rate. A real comparison with our fit value is not possible because the necessary packing density is not given for the type of experiments from which the viscosity values were estimated. The discussion of the empirical formulae (12)–(15) as well as the available experimental

results [19,36], show that viscosity measurements in *highly* concentrated hard sphere suspensions are very sensitive on experimental methods [32], the accurate determination of the density packing [33], and the type of flow involved in the measurements [37]. In the present state of the experiments, these dependencies have not been studied in detail.

The aspect ratio of the cell suggests that a description referring to the Hele-Shaw type of the cell might be closer to the experimental configuration. Adapting the dispersion relation of the Saffmann–Taylor instability to the case of zero throughflow velocity leads to [38]

$$n(k) = \frac{b^2}{12(\mu_1 + \mu_2)}[kg[\rho_2 - \rho_1) - Tk^3] , \tag{18}$$

where $b = 2 \, mm$ denotes the width of the cell. Eq. (18) contains two parameters, the dynamical viscosity μ_2 of the mixture and the surface tension T. The validity of the Hele–Shaw approach is limited by a cut-off condition at which the wave number exceeds $2\pi/b$. The fit values $\mu_2 \simeq 85\mu_1$ at $\phi = 0.603$ and $T \simeq 2.77 \times 10^{-3} \, N \, m^{-1}$ result in a fit curve which is inferior to the Rayleigh–Taylor fit (Fig. 18). Particularly a nonzero surface tension between the water–sand mixture and water is arguable.

It has to be stressed that both the Hele-Shaw and the Rayleigh–Taylor approach assume a trivial y dependence of the flow. In the experiment, that assumption is not totally fulfilled: the rotation of the apparatus leads to a sand layer which is not perfectly flat even in the beginning of the flow process (see Section 2.3).

6. Concluding remarks

In a closed Hele-Shaw-like cell the temporal evolution of a water–sand interface was investigated. For the unstable stratification, sand above water, the instability is driven by gravity. The images of the temporal evolution were analyzed by DFT. The Fourier spectra show that the initial disturbances of the interface grow exponentially at the beginning of the pattern forming process. This enables us to determine the growth rates by an exponential fit for every wave number in our spectra. The data show that the growth rate has a *nonmonotonous k* dependence: it increases steeply towards a maximum at $k \sim 11 \, cm^{-1}$. Then it passes through a flat minimum after which the growth rate increases moderately again.

To describe the general behavior we choose a two-fluid system as a model. Carrying out a linear stability analysis for the interface between the two fluids we calculate the growth rates from the dispersion relation for a finite-size cell. The theoretical results agree well with the first part in the experimental findings when using a relative viscosity of the water–sand mixture according to the empirical formula (15).

Considering our simplifications and the uncertainty in one relevant material parameter, the continuum approach gives a reasonable agreement with the experimental results: for not too large wave numbers the fluid model describes satisfactorily the experimental results. For large wave numbers the model fails to describe the measured behavior. Thus, our present results display that an analogy between concentrated suspensions and fluids can be drawn for $k \leq 15 \, cm^{-1}$. However, further investigations need to be done in order to clarify open questions.

One reason for the deviation between theoretical and experimental results at large k could be the effect of shear thinning. It describes a decreasing viscosity with increasing shear rate [39]. Modulations of the velocity over short wave lengths are associated with larger shear rates which could result in a reduced viscosity, i.e. a reduced damping and therefore an increased growth of the disturbances at large k.

The available experimental data suggest that there is no interfacial tension between the water–sand mixture and water. A surface tension acts in a way to minimize the surface of the fluid. Therefore it suppresses the formation of waves with large wave numbers because their creation entail additional surface. The suppression leads to a saturation (reduction) in the growth rates of disturbances with large (very large) wave numbers. In the context of miscible fluids with slow diffusion the concept of an effective dynamical surface tension was recently successfully applied [40]. The reason for such a surface tension lies in the attraction between moving particles in a fluid for nonzero Reynolds numbers [41]. The attraction originates from the dynamics in the viscous fluid and results in a favored distance between the moving particles. Consequently, it costs energy to separate the particles beyond this favored distance, i.e., to dilute the suspension. The necessary energy corresponds to a surface tension which is called effective *dynamical* surface tension to emphasize its dynamical origin. The effect of such an effective dynamical surface tension is seen in experiments by the presence of sharp interfaces in rising bubbles, falling drops [42] and of growing deposits [40]. A concentration gradient concerning sand and more or less sharp interfaces are present in our system which allow, in principle, the existence of a dynamical surface tension. For its determination a wide region of k values has to be covered which is realized in the presented measurements in difference to former ones [25]. The experimental results indicate that there is very likely no surface tension present.

Fluctuations of $\rho_{\text{mixture}}(\phi)$, i.e., fluctuations of the packing density ϕ, imply variations of $\mu_r(\phi)$. These would lead to terms of higher order because all terms which contain the viscosity are already linear in the velocity disturbances (see (2)–(4)). Since a linear stability analysis is restricted to terms linear in the disturbances we cannot take into account fluctuations in the relative viscosity of the mixture. This inconsistency owing to the restrictions of our linear theory can only be resolved in a nonlinear analysis.

Appendix

The matrix for finite L_z is

$$
\begin{pmatrix}
e^{-kL_z} & e^{kL_z} & e^{-q_1 L_z} & e^{q_1 L_z} & 0 & 0 & 0 & 0 \\
ke^{-kL_z} & -ke^{kL_z} & q_1 e^{-q_1 L_z} & -q_1 e^{q_1 L_z} & 0 & 0 & 0 & 0 \\
0 & 0 & 0 & 0 & e^{kL_z} & e^{-kL_z} & e^{q_2 L_z} & e^{-q_2 L_z} \\
0 & 0 & 0 & 0 & ke^{kL_z} & -ke^{-kL_z} & q_2 e^{q_2 L_z} & -q_2 e^{-q_2 L_z} \\
1 & 1 & 1 & 1 & -1 & -1 & -1 & -1 \\
k & -k & q_1 & -q_1 & -k & k & -q_2 & q_2 \\
2\mu_1 k^2 & 2\mu_1 k^2 & \mu_1(q_1^2 + k^2) & \mu_1(q_1^2 + k^2) & -2\mu_2 k^2 & -2\mu_2 k^2 & -\mu_2(q_1^2 + k^2) & -\mu_2(q_1^2 + k^2) \\
R/2 - C - \alpha_1 & R/2 + C + \alpha_1 & R/2 - q_1 C/k & R/2 + q_1 C/k & R/2 - C + \alpha_2 & R/2 + C - \alpha_2 & R/2 - q_2 C/k & R/2 + q_2 C/k
\end{pmatrix}.
$$

Furthermore, the abbreviations

$$R = \frac{k}{n^2}\left[g(\alpha_2 - \alpha_1) + \frac{k^2 T}{\rho_1 + \rho_2} \right] \tag{A.1}$$

and

$$C = \frac{k^2}{n}(\alpha_1 v_1 - \alpha_2 v_2) \tag{A.2}$$

were used.

References

[1] H.M. Jaeger, S.R. Nagel, R.P. Behringer, Rev. Mod. Phys. 68 (1996) 1259.
[2] P.B. Umbanhowar, F. Melo, H.L. Swinney, Nature 382 (1996) 793.
[3] H.A. Makse, S. Havlin, P.R. King, H.E. Stanley, Nature 386 (1997) 379.
[4] D.E. Goldsack, M.F. Leach, C. Kilkenny, Nature 386 (1997) 29.
[5] G.H. Ristow, in: D. Stauffer (Ed.), Annual Reviews of Computational Physics, Vol. I, World Scientific, Singapore, 1994, p. 275.
[6] V. Buchholtz, T. Pöschel, H.-J. Tilemans, Physica A 216 (1995) 199.
[7] G.A. Kohring, J. Phys. I (France) 5 (1995) 1551.
[8] P.K. Haff, J. Fluid Mech. 134 (1983) 401; J.T. Jenkins, M.W. Richman, J. Fluid Mech. 192 (1988) 313.
[9] J.T. Jenkins, S.B. Savage, J. Fluid Mech. 130 (1983) 187; J.T. Jenkins, J. Appl. Mech. 59 (1992) 120.
[10] H. Hayakawa, S. Yue, D.C. Hong, Phys. Rev. Lett. 75 (1195) 2328.
[11] J.J. Brey, J.W. Dufty, C.S. Kim, A. Santos, Phys. Rev. E 58 (1998) 4638.
[12] O. Pouliquen, J. Delour, S.B. Savage, Nature 386 (1997) 816; O. Pouliquen, S.B. Savage, Fingering instability in granular chute flows, preprint, 1996.
[13] H.E. Huppert, Nature 300 (1982) 427.
[14] F. Melo, P. Umbanhowar, H.L. Swinney, Phys. Rev. Lett. 72 (1994) 172; N. Mujica, F. Melo, Phys. Rev. Lett. 80 (1998) 5121.
[15] S. Fauve, K. Kumar, C. Laroche, D. Beysens, Y. Garrabos, Phys. Rev. Lett. 68 (1992) 3160.
[16] R.A. Bagnold, Proc. R. Soc. London A 225 (1954) 49; 295 (1966) 219.
[17] M. Schröter, Diploma Thesis, University of Magdeburg, 1997.
[18] A.T. Skjeltorp, in: R. Pynn, T. Riste (Eds.), Time-Dependent Effects in Disordered Materials, Plenum Press Corporation, New York, 1987, p. 71.
[19] A.K. Didwania, G.M. Homsy, Ind. Eng. Chem. Fundam. 20 (1981) 318.
[20] O.A. Druzhinin, Phys. Fluids 7 (1997) 315.
[21] X. Nie, Y.-H. Qian, G.D. Doolen, S. Chen, Phys. Rev. E 58 (1998) 6861.
[22] S.I. Voropayev, Y.D. Afanasyev, G.J.F. van Heijst, Phys. Fluids A 5 (1993) 2461.
[23] A.E. Hosoi, T.F. Dupont, J. Fluid Mech. 328 (1996) 297.
[24] D.H. Sharp, Physica D 12 (1984) 3.
[25] A. Lange, M. Schröter, M.A. Scherer, A. Engel, I. Rehberg, Eur. Phys. J. B 4 (1998) 475.
[26] Lord Rayleigh, Proc. London Math. Soc. 14 (1883) 170; G. Taylor, Proc. R. Soc. London A 201 (1950) 192; D.J. Lewis, Proc. Roy. Soc. London A 202 (1950) 81.
[27] S. Chandrasekhar, Hydrodynamic and Hydromagnetic Stability, Oxford, Univeristy Press, Oxford, 1961 (Chapter X).
[28] K.O. Mikaelian, Phys. Rev. E 54 (1996) 3676.
[29] H. Rumpf, Particle Technology, Chapman & Hall, London, 1990, p. 8.
[30] I.M. Kreiger, T.J. Dougherty, Trans. Soc. Rheol. 3 (1959) 137.

[31] J.S. Chong, E.B. Christiansen, A.D. Baer, J. Appl. Polym. Sci. 15 (1971) 2007.
[32] N.A. Frankel, A. Acrivos, Chem. Eng. Sci. 22 (1967) 169; A. Acrivos, in: M.C. Rocco (Ed.), Particulate Two-Phase Flow, Butterworth-Heinemann, Boston, 1993, p. 169.
[33] S.P. Meeker, W.C.K. Poon, P.N. Pusey, Phys. Rev. E 55 (1997) 5718.
[34] M. Ungarish, Hydrodynamics of Suspensions, Springer, Berlin, 1993, p. 17.
[35] G.Y. Onoda, E.G. Liniger, Phys. Rev. Lett. 64 (1990) 2727.
[36] L. Arnaud, C. Boutin, in: P. Moldenaers, R. Keunings (Eds.), Theoretical and Applied Rheology, Elsevier, Amsterdam, 1992, p. 640.
[37] R. Pätzold, Rheol. Acta 19 (1980) 322.
[38] P.G. Saffman, G. Taylor, Proc. Roy. Soc. London A 245 (1958) 312; K.V. McCloud, J.V. Mahler, Phys. Rep. 260 (1995) 139.
[39] C.W. Macosko, Rheology, VCH Publishers, New York, 1993 (Chapter 10).
[40] M.-Q. Lòpez-Salvans, P.P. Trigueros, S. Vallmitjana, J. Claret, F. Sagués, Phys. Rev. Lett. 76 (1996) 4062.
[41] K.O.L.F. Jayaweera, B.J. Mason, G.W. Slack, J. Fluid Mech. 20 (1964) 121.
[42] D.D. Joseph, Y.Y. Renardy, Fundamentals of Two-Fluid Dynamics, Springer, New York, 1993 (Chapter X).